High throughput spectrometer for fast localized Doppler measurements

D. Craig,[a)] D. J. Den Hartog, D. A. Ennis, S. Gangadhara, and D. Holly
The Center for Magnetic Self-Organization in Laboratory and Astrophysical Plasmas,
1150 University Avenue, University of Wisconsin-Madison, Madison, Wisconsin 53706

A new custom-built duo spectrometer has been commissioned for fast localized Doppler measurements of plasma ions in the Madison Symmetric Torus. The instrument combines very high optical throughput (transmission efficiency of 6% and etendue of 0.80 mm^2 sr divided into two simultaneous measurements) with good resolution ($\lambda/\Delta\lambda = 5600$). The design is a double grating variant of the Czerny-Turner layout and has been carefully optimized for fast (100 kHz) measurements of the C VI line at 343.4 nm. The instrument is currently being applied for high speed charge exchange recombination spectroscopy measurements. © *2007 American Institute of Physics.*
[DOI: 10.1063/1.2424450]

I. INTRODUCTION

A new custom-built duo spectrometer has been commissioned for fast localized Doppler measurements in the Madison Symmetric Torus (MST).[1] The instrument combines very high optical throughput (transmission efficiency of 6% and etendue of 0.80 mm^2 sr divided into two simultaneous measurements) with good resolution ($\lambda/\Delta\lambda = 5600$) and a high data rate (100 kHz). Typically, throughput and resolution are traded against one another in spectrometer design, and we are not aware of a commercial product with this combination of both. The design is based on a double grating variant of the Czerny-Turner layout proposed by Murty[2] and has been carefully optimized for fast measurements of near UV line profiles.

Measurements of ion velocity and temperature are important for understanding many aspects of high temperature plasmas. Mean (large spatial scale) flows play a key role in determining particle and energy transport[3] and in some cases the stability[4] of confined plasmas. Ion temperature gradients can drive instabilities and transport,[5] and the ion pressure profile is a necessary component in any analysis of plasma heat transport. Fluctuating (small spatial scale) flow velocities can cause particle or energy transport if correlated with density or pressure fluctuations[6] and can generate or modify magnetic fields through a dynamo when correlated with magnetic field fluctuations.[7]

Doppler spectroscopy is the most frequently used method for measuring ion velocity and temperature in plasmas. The emission lines of impurity ions in the plasma are Doppler shifted due to ion flow along the line of sight, and Doppler broadened due to ion thermal motions. Measurement of the wavelength shift and width of the emission lines thus provides a measure of ion velocity and temperature. Doppler measurements normally represent a path integral across the entire plasma. To obtain spatially localized measurements, emission lines can be stimulated by injecting a neutral atomic beam into the plasma. Charge exchange between the beam atoms and plasma ions creates enhanced line emission along the beam trajectory. The Doppler measurement, normally a path integral across the entire plasma, can then be localized to the region where the line of sight and neutral beam intersect. This technique is known as charge exchange recombination spectroscopy (CHERS or CXRS) and has been widely implemented in magnetic fusion devices.[8,9]

In most implementations of CHERS, the emitted light is dispersed by a spectrometer and imaged onto a charge coupled device (CCD) detector.[10–12] These systems are limited by overall throughput and detector technology to a bandwidth of ~1 kHz. To obtain faster time response (~100 kHz), higher optical throughput and fast low-noise detector technology are required. One solution which was used successfully on the Tokamak Fusion Test Reactor (TFTR) employed a high throughput interference filter spectrometer and avalanche photodiodes to record four spectral channels with high time resolution. High throughput grating systems have also been developed and applied for passive spectroscopy.[13–15] The instrument described in this article builds upon previous experience with high throughput grating instruments, improving the overall light collection by nearly two orders of magnitude over that achieved in Ref. 14.

In the following sections the spectrometer system is described in detail. In Sec. II we describe the optical layout and individual optical components in the spectrometer. In Sec. III we describe the hardware and alignment associated with the large grating mosaics used in the spectrometer. Secs. IV and V provide details on the fiber bundles that couple to the entrance and exit planes as well as the array of photomultiplier tube (PMT) detectors used for fast data collection. In Sec. VI we discuss optical ray tracing for the instrument and compare with calibration data. Sample data are discussed in Sec. VII, and in Sec. VIII we summarize.

---

a)Permanent address: Wheaton College, 501 College Ave., Wheaton, IL 60187.
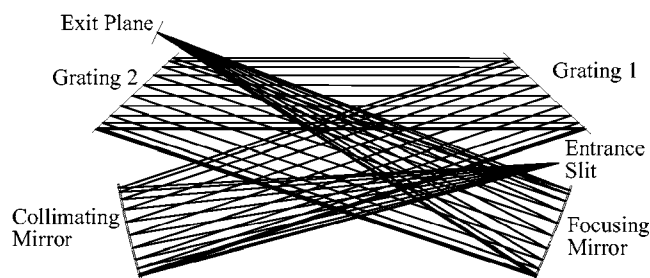
FIG. 1. Optical layout of spectrometer. Light propagates from the entrance slit to the collimating mirror, then to grating 1, grating 2, the focusing mirror, and finally to the exit plane.

II. SPECTROMETER OPTICAL COMPONENTS

The optical layout for the spectrometer is shown in Fig. 1 and a photograph of the assembled optics is shown in Fig. 2. Light emitted from the entrance slit is collimated by a spherical mirror with a focal length of 750 mm placed approximately one focal length away from the entrance slit. The collimated light is directed onto a plane diffraction grating which disperses the light in first order. The dispersed light is directed onto a second diffraction grating that further disperses the light in the first order of opposite sign, doubling the dispersion and inverting the anamorphic magnification of the first grating. The light then travels to a final spherical mirror, also of 750 mm focal length, and finally converges to form a dispersed image at the exit plane.

The collimating mirror is a simple spherical mirror with a 178 mm diameter circular aperture. After appropriately positioning the entrance slit near the mirror focal point, the system captures a light cone with $f/4.5$. The focusing mirror is also spherical but has a 280 mm circular aperture truncated to a width of 178 mm. The additional height of this final mirror enables more of the light entering the system near the top and bottom of the entrance slit to be passed on to the exit plane image. Both mirrors are first-surface mirrors with high reflectivity protected aluminum coatings, yielding a reflectivity above 90% in the near UV.

Each of the two large gratings is constructed by arranging four 110×110 mm^2 gratings in a mosaic for a total area of 220×220 mm^2. The large area is necessary due to the combined requirement of high throughput (large numerica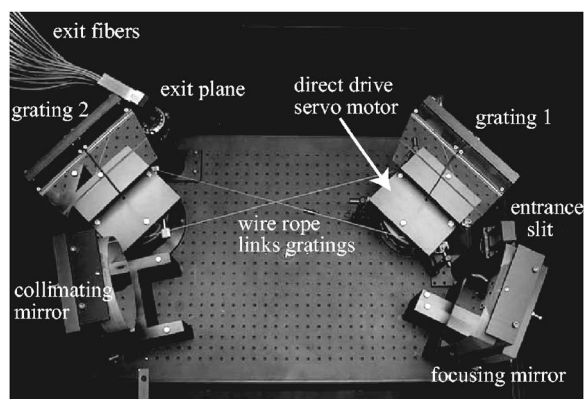l aperture) and good resolution (large focal length). The dimensions of the gratings are slightly larger than those of the spherical mirrors in order to preserve all of the light entering the instrument and to give an adequate projected area when rotated at an angle to the optical axis. Each of the smaller individual gratings is a readily available 3600 grooves/mm deeply modulated sinusoidal holographic grating from Richardson Grating Laboratories. The mosaic combination was preferred over a single 220×220 mm^2 grating because it reduces cost by a large factor and avoids the difficulties of ruling or holographically producing a grating of abnormally large size for this groove density. In addition, the diffraction limited resolving power of a single large grating was not required for this instrument. Operation in first order combined with careful grating selection results in good efficiency. The relative efficiency for unpolarized light incident on the first grating mosaic in the optical path is 55%. The gratings were chosen to have highly asymmetric efficiency curves for the two planes of polarization near the wavelength of interest (C VI line at 343 nm), which results in strongly polarized light being emitted by the first grating. The polarization is then optimal for the second grating mosaic to diffract with higher efficiency resulting in a combined efficiency of 37% for the series combination of both gratings.

The grating angles are adjusted by a pair of rotation stages. The first grating mosaic is mounted on a computer controlled motorized rotation stage, while the second grating mosaic is mounted on a free spinning stage. A wire-rope link connects the two stages in a figure eight linkage and ensures that the angle of the second grating is always equal and opposite to that of the first grating. The motorized stage is a direct drive servomotor capable of positioning the gratings with 0.005° resolution, sufficient for our application. The limiting requirement is that the emission line of interest be sufficiently centered on the exit plane detector array such that the whole line profile is captured.

III. MOSIAC GRATING ALIGNMENT

While the difficulty and cost of producing a large grating are avoided with a grating mosaic, additional complexity is added to the system because the gratings within each mosaic must be aligned relative to one another. For systems whose resolution is diffraction limited, the alignment requirements would be extreme, requiring all gratings to lie in one plane and have groove directions and spacing aligned to high precision. Since we do not operate in the diffraction limit, our requirements are less severe though still challenging. The gratings need not lie precisely in the same plane but must lie in parallel planes (requiring two angle adjustments) and have grooved directions aligned (requiring a third angle adjustment). Ray tracing analysis was used to determine the alignment mismatches that could be tolerated without significant smearing of the exit plane image due to overlap of the different images from each individual small grating in the mosaic. The limits obtained were 0.001° for the tilt that horizontally (in the dispersive direction) displaces the exit plane image, 0.01° for the tilt that vertically displaces the exit
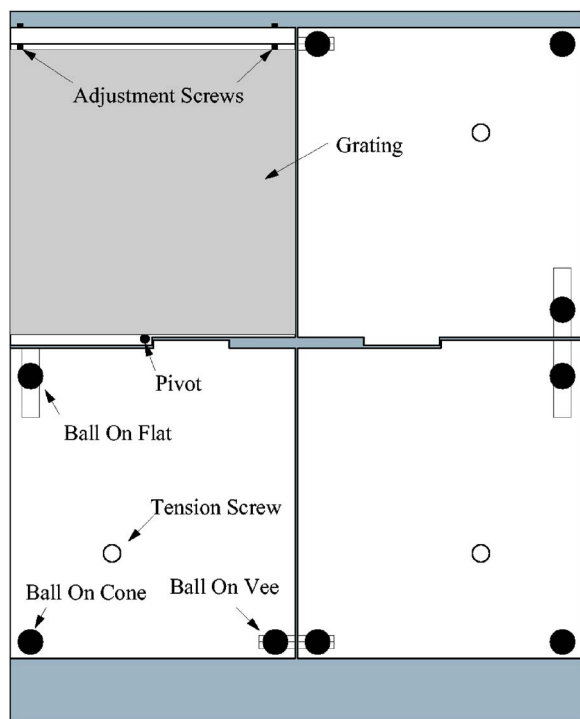

FIG. 2. Photograph of spectrometer optics.

FIG. 3. Schematic diagram of mosaic grating mount. The upper left panel shows the front side of one kinematic grating mount with grating in place. The remaining three panels show the contact points between each grating holder and the backplate which joins the four grating subassemblies together.

FIG. 4. Photographs of the spectrometer end of the entrance fiber bundles both without (a) and with (b) the entrance slit mask installed.

plane image, and 0.01° for the rotation of the grating about an axis normal to the grating surface (which determines the groove orientation).

The necessary alignment was achieved with a custom grating mount shown schematically in Fig. 3. Each individual grating is situated in a kinematic mount that includes a pair of 40 threads/in. screws and a pivot to allow rotation of the grating about an axis normal to the grating surface. The kinematic adjustments for each grating mount are made with 80 threads/in. adjustment screws with hardened ball tips used in a vee-cone-flat setup. The vee and flat are constructed from a pair of hardened stainless dowels and a carbide blank, respectively. The adjustment screws are threaded into inserts in a large mosaic backplate that holds the assembly of four gratings as one unit.

To align the tilt angles of the gratings, an autocollimator with 5 arc sec resolution was used. One grating was fixed and the other three gratings were aligned to this reference grating. A blue HeCd laser was used to align the grating groove directions along a vertical line. The plane of dispersion for each grating was made horizontal by adjusting the pair of screws on each grating mount to minimize the vertical displacement between three different orders of diffracted laser light. The tilt and rotation adjustments were iterated until a suitable alignment was obtained. The stability of the mount is evidenced by the small measured deviations of the alignment from its initial setting over a period of several months.
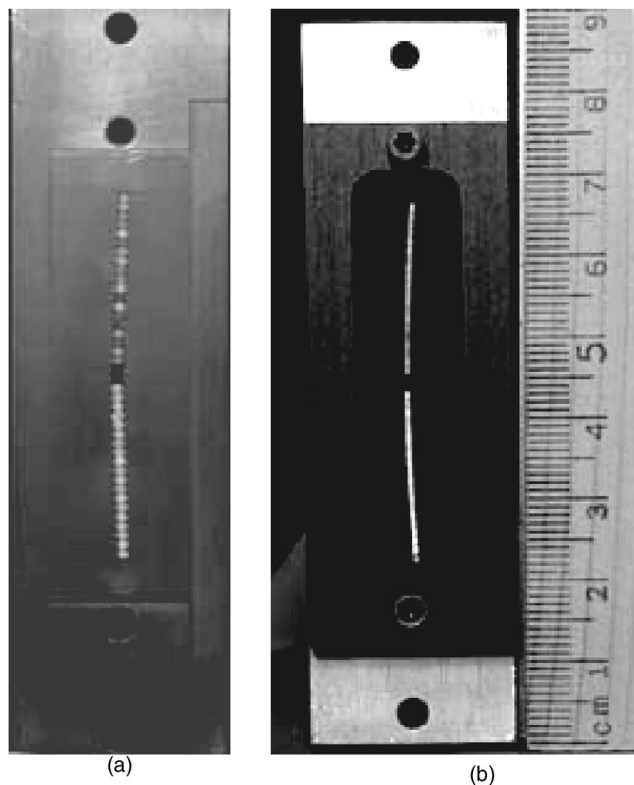
IV. ENTRANCE FIBERS AND SLITS

Light is coupled from the plasma to the spectrometer entrance plane with 3 m long fiber optic bundles. For our application, two parallel measurements are required—one of light coming from a sight line that intercepts the neutral beam, and a second from a slightly displaced sight line that collects background light without any beam-induced emission.[16,17] It is convenient to make both measurements in the same instrument in order to eliminate systematic errors that would arise in comparing the spectra from independent instruments. Hence the entrance slit is divided into upper and lower halves to accommodate the two measurements. The upper half of the entrance slit is joined to one fiber bundle and the lower half is joined to a second fiber bundle.

Each fiber bundle is composed of 19 1 mm diameter UV-grade fused silica fibers. Including surface reflections, these fibers have a transmission of 70% in the near UV. At the spectrometer end, they are stacked to produce a line bundle (see Fig. 4), while at the opposite end they are arranged in a close-packed hexagonal (or round) arrangement. The fibers are filled at $f/4.5$ to match the spectrometer, and the simple planoconvex lens used for this purpose magnifies in such a way that the spot size of the 19 fiber bundle at the location of the neutral beam is 1.4 cm. Two unused fibers are placed at the center of the pattern on the spectrometer side to isolate the two line bundles and prevent the blurred images of the upper and lower halves from overlapping at the exit plane. A 0.5 mm wide slit mask is positioned over the line of fibers resulting in two entrance slits, each of dimension of
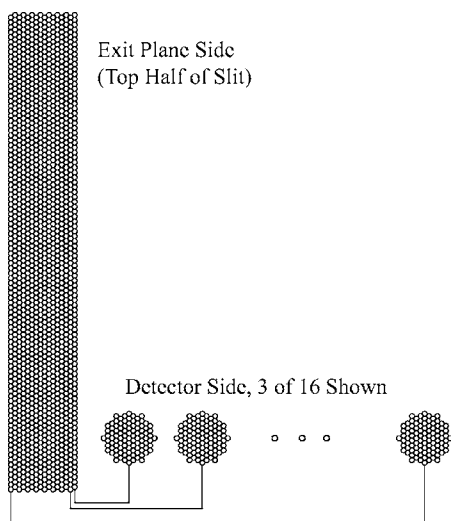
FIG. 5. Schematic diagram of exit fiber assembly for one half (upper or lower) of the exit fiber block. Each column of fibers at the exit plane converts to a round bundle which is placed in front of a PMT.

FIG. 6. Measured transfer functions for 16 of the 32 channels. The expected transfer function is shown as a dashed line for the first channel.

0.5×19 mm^2. The use of fibers of larger diameter than the slit mask width increases the packing fraction within the active area of the slit.

The slit mask is composed of two parabolic slits that overlay the two lines of fibers. The curved entrance slit compensates for a well-known imaging property that transforms a straight vertical entrance slit into a curved image at the exit plane. By introducing a curved entrance slit, the exit plane image can be made straight for one particular wavelength (i.e., one grating angle). Ray tracing analysis was used to find the curvature required for measurement of the C VI line at 343 nm, and the parabola was chosen to best fit this result. The linear stack of fibers is tilted slightly from the vertical direction with the upper and lower halves tilted in opposite directions, as shown in Fig. 4. The tilt angle of the fibers was chosen to maximize the amount of overlap between the parabolic slit and the fibers. Arranging the fibers in a parabolic shape would be more costly and is unnecessary because ample overlap exists between the wide tilted straight line bundle and the narrower parabolic slit mask.

The entrance fibers are mounted on a single axis translation stage which is oriented to move along the optical axis. Thus, focusing of the instrument is achieved by motion of the entrance plane with the first mirror kept fixed.

V. EXIT PLANE FIBERS AND LIGHT DETECTION

To achieve high speed readout of the dispersed spectra, the exit plane image is fiber optically coupled to an array of 32 photomultiplier tubes (PMTs), with 16 channels allocated to the upper half of the image and 16 to the lower half. A custom fiber bundle composed of 0.5 m long, 200 μm core/220 μm clad diameter UV-grade fused silica fibers (shown schematically in Fig. 5) is used for this purpose. Including surface reflections from the fiber ends, the transmission efficiency of the fibers is 90%. The jackets were stripped from the fiber ends to allow close packing yielding a packing fraction of about 60%. For each channel, a vertical line bundle of 96 fibers at the exit plane couples to a round
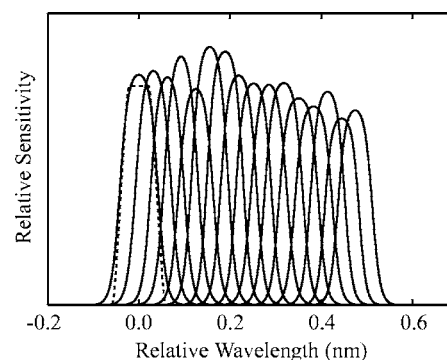
pattern that directly illuminates a PMT (model 9125Q from Electron Tubes, Inc.) Hence, each PMT measures the intensity of a small wavelength region with parallel readout and digitization of the data for fast spectral acquisition. The adjacent line bundles are closely packed with the fiber jackets stripped off to minimize packing fraction losses.

Since the exit fiber width is approximately half of the entrance slit width, the dispersed image is somewhat oversampled and the transfer functions for the exit channels overlap (see Fig. 6). Such a configuration results in an instrument with poorer wavelength resolution but actually improves accuracy for measurements of isolated lines with narrow widths (corresponding to low ion temperatures in our application). When the entrance and exit slits are of the same width, the resolution is greatest but for very narrow lines, only one or two detector channels will detect a significant amount of light. Overlapping transfer functions assure that several channels will register good signal even for very narrow lines. Modeling of the spectrometer performance with a Monte Carlo code indicates that nonlinear fits to data composed of several valid channels are more accurate and less susceptible to noise than those constrained by only one or two significant channels.

The PMTs are mounted inside a soft iron box and each PMT has a mu-metal shield to provide shielding from stray magnetic fields. The output of each PMT is amplified by a custom transimpedance amplifier with a gain of 10^6 V/A and low intrinsic noise ($<$1 mV). The amplifiers also incorporate a four-pole Bessel filter with 100 kHz corner frequency to smooth the fast response of the PMT with a constant time delay and negligible ringing. The bandpass was chosen based on an estimate of the Poisson photon counting noise for typical MST signal levels. The overall noise level during typical operation is consistent with Poisson noise which limits the temporal resolution to 10 μs at best.

VI. RAY TRACING AND CALIBRATION

Ray tracing of the complete system was performed using the ZEMAX package to examine the exit plane image quality. The two-grating setup compensates for the coma aberration at all grating angles provided that the included angles of rays reflected by the two spherical mirrors are the same. Ray tracing of a point source placed on the optical axis at the en-
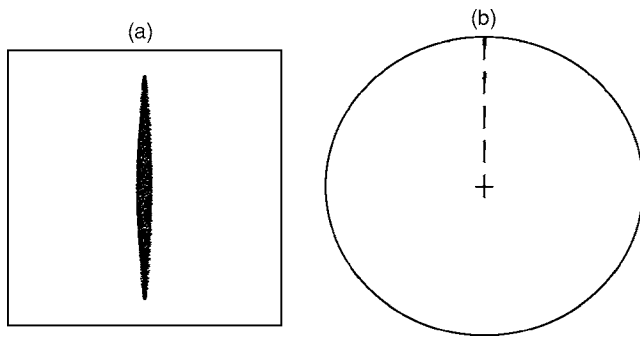
FIG. 7. (a) Spot diagram produced by light emanating from a single point at the center of the entrance plane. The box shown for scale has dimensions of 2×2 mm². (b) The spot diagram produced by rays emanating from five different points along the curved entrance slit located at heights of 0, 5, 10, 15, and 20 mm with respect to the optical axis. The good horizontal alignment illustrates correction of the slit curvature aberration.
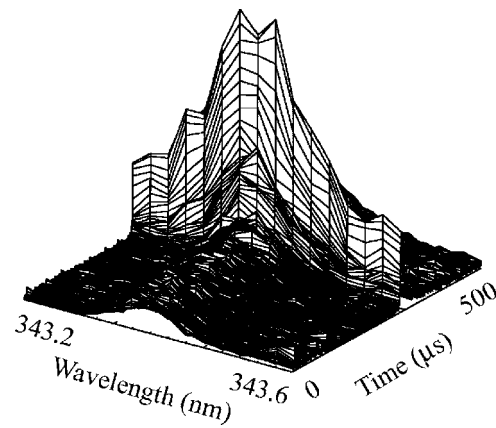

FIG. 8. Sample data for 16 of the 32 channels plotted as a function of wavelength and time. The C VI emission line at 343 nm is measured in this case.

trance plane shows that coma has indeed been eliminated, as can be seen in the symmetric spot diagram of Fig. 7(a). The dominant residual aberrations are spherical aberration and astigmatism. The amount of horizontal smearing is significantly less than the exit fiber width and the uncorrected astigmatism is not enough to cause light from the upper and lower halves of the entrance slit to mix at the exit plane. A distributed pattern of object points along the curved entrance slit also shows that the slit curvature has been corrected yielding a vertical image at the exit plane [Fig. 7(b)].

Calibration of the spectrometer wavelength setting and detector transfer functions has been performed using a Cd lamp. Light from the lamp is collected by a short focal length lens which guarantees that the spectrometer optics are completely filled. The full spectra of Cd lines in the near UV region are identified sequentially by rotating the gratings to locations for which illumination of the eighth detector channel is maximized. The pattern of these angles is matched to the wavelength pattern produced by the lamp to obtain a mapping from grating angle to wavelength. To determine the detector transfer functions, the grating angle is slowly scanned at constant velocity to sweep the pair of Cd I lines at 346.62 and 346.77 nm across the exit plane. In any one channel, the temporal separation of the intensity peaks from each line allows a conversion from time delay to wavelength difference. From this information, the transfer functions for each channel and the relative centroid position for each channel can be obtained. Transfer functions for channels 1–16 are shown in Fig. 6 along with an anticipated pattern for one channel calculated from the known spectrometer geometry and ray tracing results. The fairly good agreement between calculation and measurement (excluding differences in overall gain for each channel) indicates that the desired imaging properties have been achieved.

VII. SAMPLE DATA

A 0.5 ms slice of data taken with the spectrometer from a plasma in MST is shown in Fig. 8. The C VI line at 343 nm is measured and one can see the 16 wavelength channels covering the line profile plotted versus time. The large burst in emission in the middle of the time sequence corresponds

to a sawtooth crash during which many plasma parameters change on a rapid (100 μs) time scale. The data shown are for a line of sight which collects both background light and light produced by charge exchange with the neutral beam. A similar set of data (not shown) is collected with the other input fiber bundle from a slightly displaced line of sight which collects only background light.

The measured line profiles from the two sight lines are fitted with a model[18] to extract the carbon ion flow and temperature with fits to the background light producing line-averaged quantities and fits to the beam-induced charge exchange emission yielding spatially localized values. Figure 9 shows the results of such a fitting for a typical discharge. In MST the ion temperature can change quickly during a sawtooth crash, and the fast transition is resolved in both the line-averaged passive measurement and the spatially localized CHERS measurement. The error bars shown in Fig. 9 represent the range of fitted temperatures derived by varying each data point within the range expected from photon counting statistics and performing the fit many times. The passive measurement benefits by having many more photons than the CHERS measurement, and hence can be fitted at a higher frequency with good single shot error bars. One can see that the high throughput allows the temperature evolution to be well resolved in a single shot.
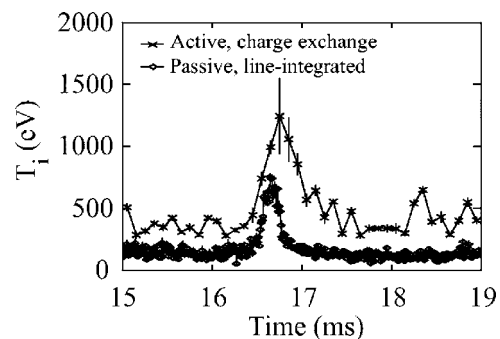

FIG. 9. Processed data showing the measured ion temperature resolved through a fast sawtooth event in MST. The passive, line-integrated data (diamonds) are fit at 10 μs intervals and the active data from charge exchange recombination (crosses) are fit at 100 μs intervals. Error bars represent uncertainties due to photon counting statistics.

VIII. SUMMARY

A custom spectrometer with very high throughput and good resolution has been constructed for fast localized Doppler measurements in MST. The two-grating instrument has been optimized for light collection in the near UV, with the C VI line at 343 nm of primary interest. The combined transmission efficiency of light collection optics, entrance fiber bundles, spectrometer optics, and exit fiber bundles is 6%. Large focal length (750 mm) and large aperture ($f/4.5$) force the use of large optics. A grating mosaic with four 110 ×110 mm^2 gratings has been used in place of a large single grating to reduce cost and enlarge the domain of potential suppliers. The system is now being used to examine fast ($\sim$100 μs) changes in ion flow and temperature and also to measure ion fluctuations in MST.

ACKNOWLEDGMENTS

[1] R. N. Dexter, D. W. Kerst, T. W. Lovell, S. C. Prager, and J. C. Sprott, Fusion Technol. **19**, 131 (1991).
[2] M. V. R. K. Murty, Opt. Eng. (Bellingham) **13**, 23 (1974).
[3] R. J. Groebner, K. H. Burrell, and R. P. Seraydarian, Phys. Rev. Lett. **64**, 3015 (1990).
[4] M. S. Chu, J. M. Greene, T. H. Jensen, R. L. Miller, A. Mondeson, R. W. Johnson, and M. E. Mauel, Phys. Plasmas **2**, 2236 (1995).
[5] W. Horton, Rev. Mod. Phys. **71**, 735 (1999).
[6] N. E. Lanier *et al.*, Phys. Plasmas **8**, 3402 (2001).
[7] D. J. Den Hartog, J. T. Chapman, D. Craig, G. Fiksel, P. W. Fontana, S. C. Prager, and J. S. Sarff, Phys. Plasmas **6**, 1813 (1999).
[8] R. C. Isler and L. E. Murray, Appl. Phys. Lett. **42**, 355 (1983).
[9] R. J. Fonck, D. S. Darrow, and K. P. Jaehnig, Phys. Rev. A **29**, 3288 (1984).
[10] R. E. Bell, L. E. Dudek, B. Grek, D. W. Johnson, and R. W. Palladino, Rev. Sci. Instrum. **70**, 821 (1999).
[11] P. G. Carolan, N. J. Conway, C. A. Bunting, P. Leahy, R. O'Connell, R. Huxford, C. R. Negus, and P. D. Wilcox, Rev. Sci. Instrum. **68**, 1015 (1997).
[12] K. H. Burrell, P. Gohil, R. J. Groebner, D. H. Kaplan, J. I. Robinson, and W. M. Solomon, Rev. Sci. Instrum. **75**, 3455 (2004).
[13] H. T. Evensen, R. Durst, R. J. Fonck, and S. F. Paul, Rev. Sci. Instrum. **66**, 845 (1995).
[14] D. J. Den Hartog and R. J. Fonck, Rev. Sci. Instrum. **65**, 3238 (1994).
[15] R. A. Bamford, P. G. Carolan, and C. A. Bunting, Rev. Sci. Instrum. **63**, 4962 (1992).
[16] D. Craig, D. J. Den Hartog, G. Fiksel, V. I. Davydenko, and A. A. Ivanov, Rev. Sci. Instrum. **72**, 1008 (2001).
[17] D. J. Den Hartog *et al.*, Rev. Sci. Instrum. **77**, 10F122 (2006).
[18] S. Gangadhara, D. Craig, D. A. Ennis, and D. J. Den Hartog, Rev. Sci. Instrum. **77**, 10F109 (2006).